



An ingenious construction of porous sodium alginate/TEMPO-oxidized cellulose composite aerogels for efficient adsorption of crystal violet dyes in wastewater

Zhao Zhang¹ · Kun Li¹ · Wenjie Dong¹ · Zihao Wang¹ · Xinyan Zhang¹ · Jikui Wang¹

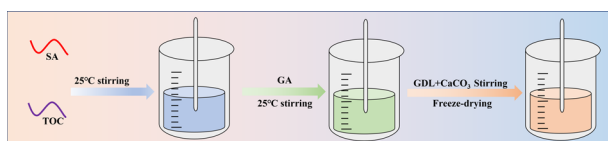
Received: 30 October 2023 / Accepted: 14 December 2023 / Published online: 25 March 2024

© The Author(s), under exclusive licence to Springer Science+Business Media, LLC, part of Springer Nature 2024

Abstract

Since caustic dyes are a major component of wastewater used in printing and dyeing, they represent a significant risk to human health. It's getting harder to get rid of them efficiently. An appealing solution to this issue is adsorption based on biomass material aerogel. Here, using the sol-gel process and freeze-drying, an inventive three-dimensional porous aerogel (STA) was created using sodium alginate (SA) and TEMPO-oxidized cellulose (TOC) as raw materials, with the dual cross-linking effects of glutaraldehyde (GA) and Ca^{2+} . Various characterization approaches and analytical methods were used to study STA. The results indicated that the addition of TOC resulted in the excellent pore structure, thermal stability, charge characteristic and adsorption capacity of STA. The adsorption capacity of STA was investigated by selecting crystalline violet (CV) as a typical cationic dye. Thereafter, the adsorption capacity was comprehensively analyzed by varying temperature, pH and adsorption time. The adsorption process conformed to the pseudo-second-order kinetic model, and the Langmuir isothermal adsorption model has a better fit, which was a single-molecule layer chemisorption process. The highest adsorption capacity reached 505.9 mg/g. Moreover, STA also possessed outstanding competitive adsorption capacity and cyclic adsorption performance.

Graphical Abstract



Keyword Sodium alginate · TEMPO-oxidized cellulose · Aerogel · Crystal violet · Adsorption

Highlights

- Sodium alginate and TEMPO-oxidized cellulose were combined innovatively, and the application scope of bio-based materials was expanded.
- A double cross-linking reaction was achieved in the presence of Ca^{2+} and glutaraldehyde.
- The largest porosity reached 95.6% as a result of the three-dimensional porous structure.
- The maximum adsorption capacity for CV reached 505.98 mg/g. Recycling times and competitive adsorption capacity are excellent.
- The thermal stability was enhanced to some extent due to the addition of TOC.

✉ Jikui Wang
wang326@ecust.edu.cn

School of Materials Science and Engineering, East China University of Science and Technology, Shanghai 200237, People's Republic of China

¹ Shanghai Key Laboratory of Advanced Polymeric Materials, Key Laboratory for Ultrafine Materials of Ministry of Education,

1 Introduction

The more rapid growth of society has coincided with the flourishing of industrial development [1]. Simultaneously, major environmental problems have been brought about by the wastewater overflow from industrial activity [2]. Wastewater from printing and dyeing operations is one of the main sources of this hazardous wastewater, which has a significant carcinogenic effect and a large amount of released organic contaminants [3]. Because most organic dyes have cyclic structures, they are difficult to remove and stable in water bodies [4]. The main methods for treating dyeing wastewater include chemical coagulation, solvent extraction, biochemical treatment, membrane separation, adsorption, and other methods [5]. The adsorption process includes exposing a porous adsorbent to wastewater and then transferring the pollutants to the adsorbent via physical or chemical adsorption [6]. This method is extremely efficient, easy to use, affordable, good at recycling, green, and pollution-free. It may also remove contaminants that are difficult for biodegradation [7]. Thus, one of the most effective and innovative ways to deal with the significant environmental problem is adsorption [8].

Due to its exceptional qualities, including its extremely low density, ultra-high specific surface area, and good chemical stability, aerogel has been used extensively as a three-dimensional porous material in sensors, energy storage, electromagnetic shielding, flame retardant, medical materials, supercapacitors, and other fields [9]. Additionally, aerogel has demonstrated potential for use in the adsorption field [10]. Because of its high specific surface area, robust adsorption capacity, and quick adsorption rate, it is regarded as one of the most effective adsorption materials [11]. Even so, the usage of high-performance activated carbon materials has been severely constrained by their high cost and non-biodegradability [12]. Therefore, it is critical to produce plentiful, affordable, and environmentally friendly adsorbent materials. Bio-based materials adsorbents in particular have drawn significant interest due to their biocompatibility, high degradability, and cheap cost [13].

SA is a helpful marine polysaccharide that is widely used in the food, medical, and water treatment sectors, among others. It is created through the microbial fermentation of certain bacteria found in brown algae, including seaweed, kelp, bay grass, and vesicular algae [14]. It is also widely used in the adsorption sector because of its great biodegradability, good biocompatibility, eco-friendliness, and low cost [15]. SA-produced aerogel is often considered one of the best options for removing dye contamination from water bodies because of its abundance of carboxyl (-COOH) and hydroxyl (-OH) groups that could link to dye molecules [16]. Nevertheless, pure SA aerogels have poor mechanical and thermal stability, which limits their application in water treatment [17]. Through alteration, SA's stability and

adsorption capacity can be increased and its use in water treatment can be expanded [18].

Apart from its low density, strong strength, and excellent dispersibility, cellulose is a bio-based material that is particularly abundant and renewable [19]. The high -OH content of cellulose and its derivatives makes them useful for filtering out impurities from water. Although both SA and nanocellulose are bio-based materials, SA aerogel is more advantageous to employ because of the greater performance of cellulose nanofiber (CNF) [20]. through the use of ionic cross-linking and bidirectional freeze-drying to combine CNF and SA. Liu [21] created a CNF/SA aerogel with remarkable mechanical properties and a large adsorption quantity. Yang [22] employed CNF that had been bidirectionally frozen and strengthened with SA aerogel. The experimental study showed that the synthesized aerogel owned outstanding elasticity and the adsorption capacity was increased. Chemical cross-linking and silane modification were carried out.

TOC is one of the most significant components of CNF. In addition to its large specific surface area, mechanical properties, water solubility and biodegradability, it has other unique qualities. The most notable of these is that it is rich in -COOH and -OH, making it extremely hydrophilic and easily adsorbs cationic dyes. The opportunity exists to increase the tensile strength and adsorption capability of SA adsorbent materials with the addition of TOC [23].

In this study, we used two more common bio-based materials as precursors and then skillfully combined them by double cross-linking. The abundant carboxyl groups can better adsorb the cationic dyes and thus have a higher adsorption capacity. This is a novel idea in the field of bio-based material aerogels.

Consequently, using a sol-gel method, a three-dimensional porous aerogel containing SA and TOC as the matrix and Ca^{2+} and GA as the cross-linking agents allowed for a thorough examination of the reaction process. Following that, various analytical techniques were used to examine the microstructure, chemical characteristics, thermal stability, porosity, and charge characteristic of STA. Furthermore, a thorough examination of STA's adsorption performance was conducted by the modification of experimental parameters and the use of kinetic and adsorption isotherm models. At the conclusion of this work, the competitive experiment, the cyclic adsorption experiment, and the adsorption process were also covered. As a result, a theoretical foundation for STA's extensive applicability was created.

2 Experimental section

2.1 Materials

SA (M/G ratio 1.5–1.7) was bought from Shanghai McLean Biochemical Technology Co., Ltd; TEMPO-Oxidized

nanocellulose (92.53% cellulose and 7.47% hemicellulose, Length of 20–30 μm , diameter of 15–25 nm, the degree of oxidation was as high as 91%. Derived from natural wood pulp plant fiber) was obtained from Shanghai Naicheng Biotechnology Co., Ltd; Glutaraldehyde was provided by Shanghai Yinghan Chemical Technology Co., Ltd; D-gluconic acid δ -lactone (GDL) was obtained from Shanghai Zhonghe Chemical Technology Co., Ltd; Calcium carbonate was obtained from Shanghai Naicheng Biotechnology Co., Ltd; Hydrochloric acid (HCl) and sodium hydroxide (NaOH) are obtained from Shanghai McLean Biotechnology Co., Ltd., crystal violet was provided by Shanghai Naicheng Biotechnology Co., Ltd., The materials are all analytical grade and do not need further treatment. Deionized water is prepared by our own lab.

2.2 Preparation of STA

Firstly, 10 g of SA solution with 2 wt% concentration and TOC solution with different concentrations were configured and stirred at 25 $^{\circ}\text{C}$ for 1 h. Then the two solutions were mixed and 0.5 mL of GA with a concentration of 50% was added and stirred continuously for 1.5 h to form a homogeneous co-mingled liquid named A. Next, 0.1 g of GDL was introduced into to A and stirred continuously for 30 min and sonicated for 30 min to obtain co-mingled liquid named B. Afterwards 0.05 g CaCO_3 was weighed and added to solution B, stirred uniformly to obtain a homogeneous mixed liquid named C. Next, C was quickly poured into the mold and left for 1 h to fully react, then deionized water was used to wash several times to remove excess Ca^{2+} named D. Thereafter, D was cryogenically frozen for 24 h, followed by freeze-drying at -50°C for 48 h to obtain a porous aerogel named STA. Depending on the

concentration of TOC, they are named STA-x. For example, STA-0.25 means the concentration of TOC is 0.25%. The aerogel without the addition of TOC was synthesized following similar steps as above and named SA/GA. The synthesis procedure of STA was presented in Fig. 1a.

2.3 Characterizations

The molecular structure of the aerogels was analyzed by using a Fourier transform infrared (FTIR) spectrometer, model Nicolet iS50, manufactured by Thermoelectric Corporation, USA. The crystal type of aerogels was analyzed by using an X-ray diffractometer (XRD) model Ultima IV manufactured by RIKEN, Japan, with a scanning speed of $4^{\circ}/\text{min}$ and an angular range of 5 to 75 degrees. The samples were analyzed by using an X-ray photoelectron spectrometer (XPS) model AXIS-ULTRA DLD manufactured by Shimadzu Corporation, Japan. The microstructure of the aerogel was studied by using a scanning electron microscope (SEM) model S-4800N from Hitachi, which required gold spraying prior to testing. The thermal stability of the aerogels was determined using a thermogravimetric chromatography-mass spectrometer (TG) model TG209F1-GC from NETZSCH, Germany. The potential of aerogels was analyzed by using a multi-angle particle size and Zeta potential analyzer model STABINO from Germany, and the material was subjected to high-speed shear treatment prior to the test. The absorbance of different solutions was measured by UV-Vis spectrophotometer (UV-5200 Shanghai Yuanxi Instruments Co., Ltd.).

2.4 Density and porosity tests

Because of rich pore structure, the density of aerogel has two kinds of density, the body density and the skeleton

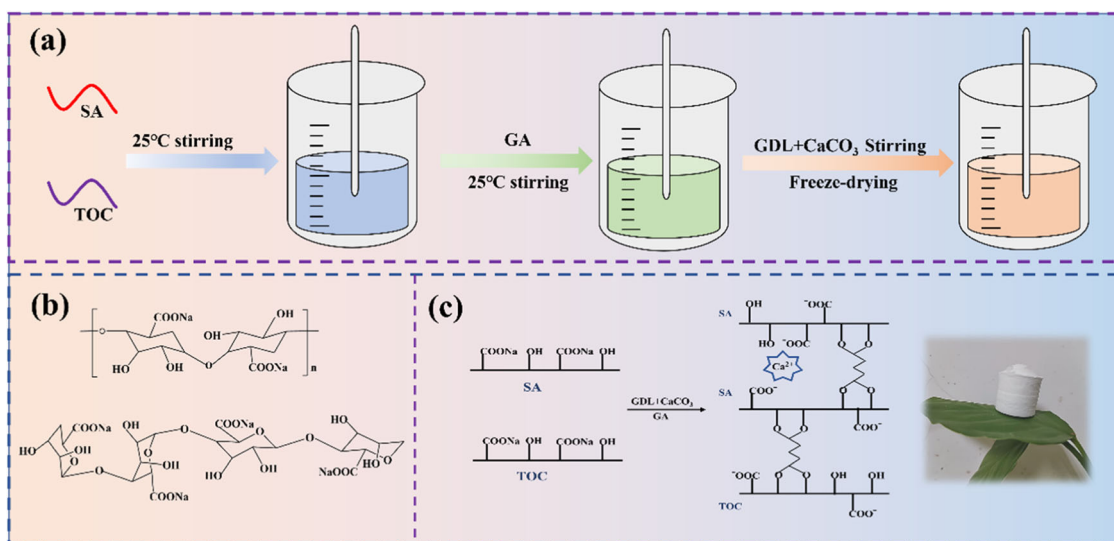


Fig. 1 a Preparation process of STA; (b) Structural formula of SA and TOC; (c) Reaction mechanism of synthesized STA

density. The bulk density is calculated by the following equation:

$$\rho_b = m_0/v \quad (1)$$

In the above equation, ρ_b represents the bulk density, m_0 indicates the mass of the aerogel to be measured, and v denotes the volume of the aerogel to be measured.

The aerogel skeleton density is tested by the specific gravity bottle method. It is calculated by the following formula:

$$\rho_s = \frac{m_0}{M_1 + m_0 - M_2} \quad (2)$$

ρ_s represents the skeleton density, m_0 shows the mass of the aerogel to be measured, M_1 is the mass of the specific gravity bottle and water, and M_2 indicates the total mass of the specific gravity bottle and water after adding the sample to be measured [24]. Each operation was repeated three times and the average value was taken.

The porosity can be calculated by the following equation:

$$P = \left(1 - \frac{\rho_b}{\rho_s}\right) \times 100\% \quad (3)$$

In this equation, P represents porosity, ρ_b denotes bulk density, ρ_s indicates skeleton density.

2.5 Adsorption experiments

In an attempt to research the adsorption capacity of STA as an adsorbent for cationic dyes, we selected CV ($C_{25}H_{31}N_3$) as a typical dye contaminant for a systematic adsorption experimental study. Firstly, a standard curve was plotted and a concentration of 1000 mg/L of CV solution was configured. Then a certain amount of CV master batch was weighed and diluted to 2 mg/L, 4 mg/L, 7.5 mg/L, 8.0 mg/L, and 10.0 mg/L. Its absorbance was measured using an UV-vis spectrophotometer in the wavelength range of 200–850 nm, respectively.

To investigate the influence of various experimental conditions on the adsorption performance, it was necessary to change the experimental conditions for the adsorption experiments [25]. Firstly, 20 mg of STA was selected as the adsorbent and 100–150 mL of dye solution was used as the contaminant. Then the effects of ambient temperature (10–50 °C), adsorption time (30–900 min), pH (2–11) and different initial concentrations (100–500 mg/L) on the adsorption effect were investigated separately. The system needed to be shaken during the adsorption process to achieve adequate adsorption. The pH of the solution was adjusted by 0.1 mol/L HCl and 0.1 mol/L NaOH, respectively. Before and after adsorption, the absorbance of the upper liquid was measured using an UV-Vis spectrophotometer and the concentration was concluded from the

standard curve so that the adsorption amount could be derived [26]. The adsorption kinetic curves and adsorption isotherms were plotted based on the above experimental results. Cyclic adsorption experiments are performed by washing and freeze-drying the adsorbed aerogel with dilute acid and deionized water before performing the next set of experiments. Cyclic adsorption experiments were performed in a solution of pH = 7 and $C_0 = 150$ mg/L when the ambient temperature was 30 °C [27].

For the adsorption experiments, the adsorption volume and the adsorption rate can be calculated by the below equations:

$$Q_e = \frac{(C_0 - C_e) \times V}{M} \quad (4)$$

$$R_e = \frac{C_0 - C_e}{C_e} \quad (5)$$

In the above two equations, Q_e denotes the adsorption amount of CV by the adsorbent when the adsorption process reaches equilibrium. R_e denotes the adsorption rate of CV by the adsorbent. C_0 represents the original concentration of the CV solution. C_e represents the concentration of the CV solution after adsorption. V represents the volume of the CV solution. M denotes the mass of the adsorbent (STA) added.

In the adsorption process, it is essential to analyze and explore the kinetics of the adsorption process, which can describe the time required to reach the adsorption equilibrium more objectively [28]. The equations of the pseudo-first-order kinetic model and pseudo-second-order kinetic are expressed as follows [29]:

$$\ln(Q_e - Q_t) = \ln Q_e - K_1 t \quad (6)$$

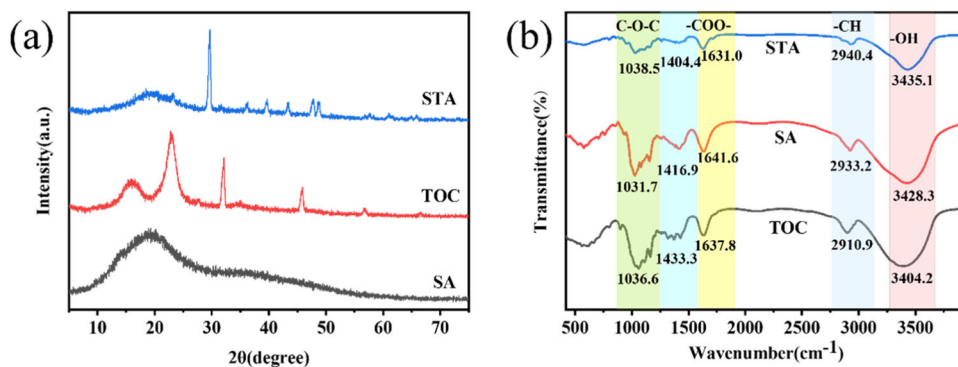
$$\frac{t}{Q_t} = \frac{1}{K_2 \times Q_e^2} + \frac{t}{Q_e} \quad (7)$$

In the above equations, the Q_e denotes the amount of adsorption of CV by the adsorbent when the adsorption reaches equilibrium (mg/g), Q_t denotes the adsorption amount of CV by the adsorbent when the adsorption time is t (mg/g), t indicates the adsorption time of the adsorbent on the CV (min), K_1 denotes the adsorption rate constant (min^{-1}), K_2 denotes the adsorption rate constant ($\text{g}/(\text{mg}\cdot\text{min})$).

The adsorption isotherm is a critical tool to examine the mechanism of adsorption between adsorbent and adsorbate and a parameter to determine the mode of interaction [30]. The expression equations of Langmuir and Freundlich isotherm adsorption model are shown below:

$$\frac{C_e}{Q_e} = \frac{C_e}{Q_m} + \frac{1}{K_L \times Q_m} \quad (8)$$

Fig. 2 a XRD patterns of different reactants in STA; (b) FTIR spectra of different substances



$$\ln Q_e = \ln K_F + \frac{1}{n_F} \ln C_e \quad (9)$$

In the above equations, C_e denotes the concentration of CV solution (mg/L) when the adsorption process equilibrium state is reached, Q_e indicates the adsorption amount of CV by the adsorbent when the adsorption reaches equilibrium (mg/g), Q_m indicates the maximum adsorption amount of CV by the adsorbent (mg/g), K_L denotes the Langmuir isothermal adsorption model constant, K_F denotes Freundlich adsorption isotherm model constant. $1/n_F$ indicates how easy it is for the adsorbent to produce adsorption on the adsorbent. When $1/n_F$ is greater than 0.1 and less than 0.5, it means that the adsorption process is relatively easy to occur, and when $1/n_F$ is greater than 2, it implies that the adsorption of the adsorbent on the adsorbent is relatively difficult [31].

In addition to the above equation, the adsorption of Langmuir adsorption model can be characterized by R_L , which can be calculated by the following equation:

$$R_L = \frac{1}{1 + K_L \times C_0} \quad (10)$$

R_L indicates how easy it is for the adsorbent to produce adsorption on the adsorbent, and when R_L is equal to 0, the adsorption process is classified as irreversible adsorption; when R_L is less than 1 and greater than 0, it means that this adsorption process is relatively easy to occur; when R_L is equal to 1, it means that the process is linear adsorption, and when R_L is greater than 1, it means that the process is not easy to occur [32].

3 Results and discussion

3.1 Analysis of the reaction mechanism

The structural formulae for TOC and SA are shown in Fig. 1b. It was discovered that both molecules had a lot of -OH and -COOH and that their molecular structures were

similar. This particular structure offered the conditions needed for the successful production of porous aerogel. The STA-making procedure was depicted in Fig. 1c. Ca^{2+} employed ionic cross-linking to establish a more stable network structure between SA when GDL, CaCO_3 , and GA were added to the mixture. When the $\text{C}=\text{O}$ in GA combined with the -OH of SA and TOC to produce an acetal structure, another layer of cross-linked network structure was formed. Excellent mechanical characteristics and good stability made this structure a solid foundation for STA. The groundwork for the excellent adsorption of cationic dyes was created by the successful creation of porous aerogel with a three-dimensional pore structure, exceptional mechanical qualities and efficient adsorption. [33].

3.2 XRD analysis

XRD can be used to examine a substance's crystal structure [34]. The XRD patterns of SA, TOC, and STA-1.0 were displayed in Fig. 2a. A packet peak at the position of $2\theta = 19.2^\circ$, which was an amorphous structure belonging to SA, could be seen in the spectrum of SA, indicating that SA was in an amorphous state. The cellulose diffraction peaks at $2\theta = 16.1^\circ$ and $2\theta = 23.2^\circ$, which belonged to the type I crystalline form of cellulose and corresponded to the (110) and (200) crystallographic planes of TOC, were clearly visible in the diffraction pattern of TOC. Next, the leftover sodium ions in TOC were identified by the diffraction peak at $2\theta = 23.2^\circ$. Comparatively, it could be said that the diffraction peaks of TOC in the XRD pattern of STA essentially vanished, while the intensity of the diffraction peaks of SA also diminished somewhat. It was clear from the phenomenon that TOC and SA had been successfully cross-linked. Incompletely reacted Ca^{2+} was present, which is why smaller diffraction peaks at 2θ of 29.7° , 39.6° , 43.4° , and 47.5° emerged. The aforementioned discussion further shown that SA and TOC and Ca^{2+} interacted to produce new compounds [35].

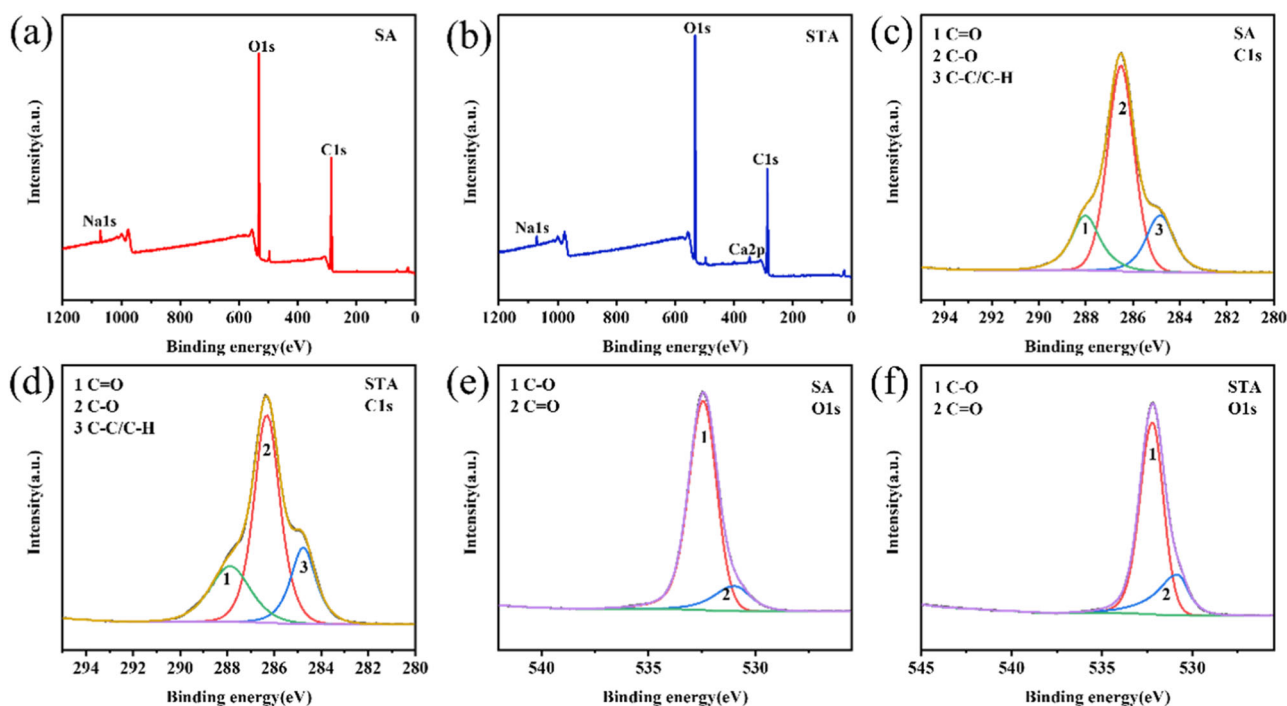


Fig. 3 a, b Full spectrum scans of SA and STA; (c, d) The XPS C1s spectra of SA and STA; (e, f) The XPS O1s spectra of SA and STA

3.3 FTIR spectra analysis

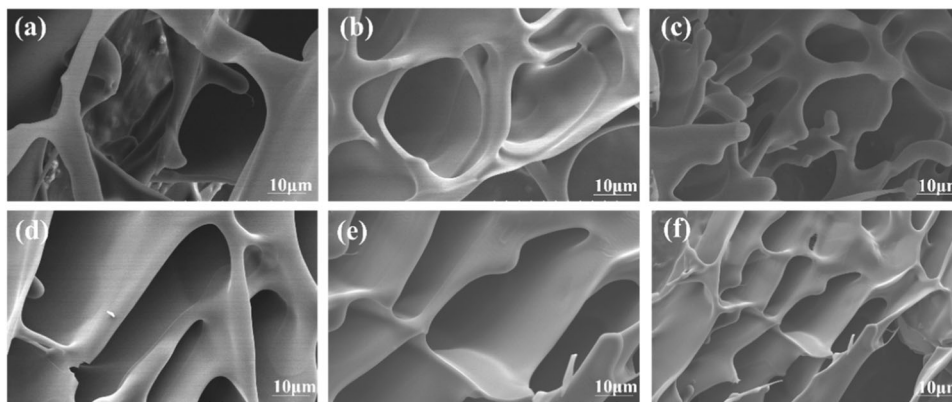
To investigate the effect of TOC on STA, we used FTIR to study the mechanism of cross-linked network structure development. First, we compared the FTIR of STA-1.0, TOC, and SA. Given their almost identical chemical structures, SA and TOC showed several comparable spectral peaks, as shown in Fig. 2b. The peaks at -OH, -CH, and -COOH that are 3428.3 or 3404.2 cm^{-1} , 2933.2 or 2910.9 cm^{-1} , and 1641.6 or 1637.8 cm^{-1} , respectively, are the stretching vibration peaks. Similar peaks also showed up in the STA infrared spectra in response. However, by careful observation, it was easy to see that the peaks of -OH and -COOH in STA were shifted, which precisely indicated the cross-linking reaction of GA with the -OH of SA and TOC. Above reasons resulted in the reduction of the -OH content, in addition to the reduction of the -COOH content in SA due to the involvement of Ca^{2+} . Concomitantly, the position of -COOH in STA was shifted. The involvement of hydrogen bonding also contributed to this phenomenon. The shifted position of -CH was also attributed to the “egg box structure” formed by the Ca^{2+} and SA, which limited the stretching vibration of -CH. The peaks at 1038.5 cm^{-1} , 1031.7 cm^{-1} , and 1036.6 cm^{-1} belong to -COC- of the three substances, respectively. It was obvious that the wavelength of -COC- was shifted in STA, which was able to be one of the evidence for the reaction between GA and -OH [36].

3.4 XPS spectra analysis

XPS tests and studies were carried out on SA and STA-1.0 to further ascertain the manner of binding between SA, TOC, and Ca^{2+} . Figure 3a, b displays the entire spectrum analysis of the SA and STA tests. Both spectra comprised C, O, and Na, which were also the primary components of aerogel, as could easily be seen. The difference was that the oxygen element content stayed higher and the O1s peak of the STA remained sharper, indicating that the TOC addition had increased the proportion of oxygen in the aerogel. More visibly, the ionic cross-linking process between Ca^{2+} and SA resulted in peaks of Ca2p on the plots of STA, retaining some Ca^{2+} in STA. It assisted in the gel network’s development [37].

The XPS spectrum of SA could be divided into three peaks by split-peak fitting, which were 286.51 eV, 284.8 eV, and 288.1 eV, respectively; in contrast, the split-peak result of STA has changed somewhat, and the binding energy of C = O and C-O has shifted, as shown in Fig. 3c–f for the C1s and O1s of SA and STA, respectively. A portion of the -COOH and -OH were consumed throughout the reaction, -COOH and Ca^{2+} underwent an ionic cross-linking reaction, and -OH coupled with GA through double bond opening, according to this result. As a result, the density of the external electron cloud increased, which also showed that SA and TOC had some hydrogen bonding interaction. The area of the C-O peaks dropped while the

Fig. 4 a–f The SEM images of SA/GA, STA-0.25, STA-0.5, STA-1.0, STA-1.5, STA-2.0



areas of the C = O and C-C peaks rose when compared to the area of each peak. According to the findings, the cross-linking reaction between -OH and GA occurred during the synthesis of STA, which led to a drop in its concentration. Toc was added to synthesized STA to increase the fraction of C = O and C-C in the system, which also provided the theoretical framework for additional adsorption experiments [38].

3.5 Morphology and microstructure analysis

The prepared aerogels' SEM pictures are shown in Fig. 4a–f. As demonstrated in Fig. 4a, which showed the aerogel without the addition of TOC, the SA distribution was not uniform and the resulting aerogel did not show a more pronounced pore structure when TOC was not added. After adding TOC, the aerogels displayed unique three-dimensional network topologies. These network structures were produced by a cross-linking reaction between the -OH in SA and the -OH in TOC and GA. Furthermore, the presence of Ca^{2+} allowed SA to design “egg box” network designs. The formation of these three-dimensional porous structures provided the perfect conditions for the growth of a specific surface area and the adsorption of tiny molecules. When the TOC concentration was 1%, the pore structure showed a narrow channel with a more distinct interface, and the strong pore wall also provided high mechanical capabilities. But as the addition of TOC exceeded 1%, the STA network became more crowded and confused. As the amount of TOC added increased, the excessive addition caused fragmentation to become more severe. As a result, some TOC did not fully respond to SA. Meanwhile, the absence of Ca^{2+} from the reaction was one of the reasons for this occurrence. The internal diffusion of dye molecules and the enhancement of porosity were both severely hampered by this. Thus, 1% TOC is a more desired addition level, which will also be confirmed in further studies [39].

Table 1 Density and porosity of different aerogel

Sample	Bulk density (g/cm ³)	Skeleton density (g/cm ³)	Porosity (%)
SA/GA	0.1523	1.436	89.4
STA-0.25	0.1163	1.571	92.6
STA-0.5	0.09438	1.714	94.5
STA-1.0	0.08751	1.988	95.6
STA-1.5	0.09372	1.511	93.8
STA-2.0	0.10265	1.445	92.9

3.6 Density and porosity analysis

The density and porosity of aerogels are shown in Table 1. It can be visualized that SA/GA showed the highest bulk density and the lowest porosity. After the addition of TOC, the density of STA exhibited a trend of decreasing and then increasing, while the porosity demonstrated a growth and then decreasing trend. However, it was more advantageous compared with the aerogel without TOC addition, and the best structure was STA-1.0, whose bulk density was 0.08751 g/cm³ and the maximum porosity was 95.6%. With the addition of TOC, the skeleton strength of the composite aerogel became stronger, and the formed network structure was more complete and stronger. This reason contributed to the above phenomenon [40].

3.7 Thermal stability analysis

Thermogravimetric studies on SA/GA aerogels and STA were carried out in order to examine the impact of TOC addition on the thermal stability performance of aerogels [41]. The findings of the experiment are displayed in Fig. 5a, b below. The first weight loss range showed at 30–200 °C, and the mass loss at this stage primarily resulted from the heat volatilization of the bound water inside the aerogel. It was discovered that the thermogravimetric analysis curves of both SA/GA and STA exhibited three main weight loss temperature ranges. The breakdown of cross-linked bonds, thermal degradation,

Fig. 5 a, b The TG images of SA/GA and STA

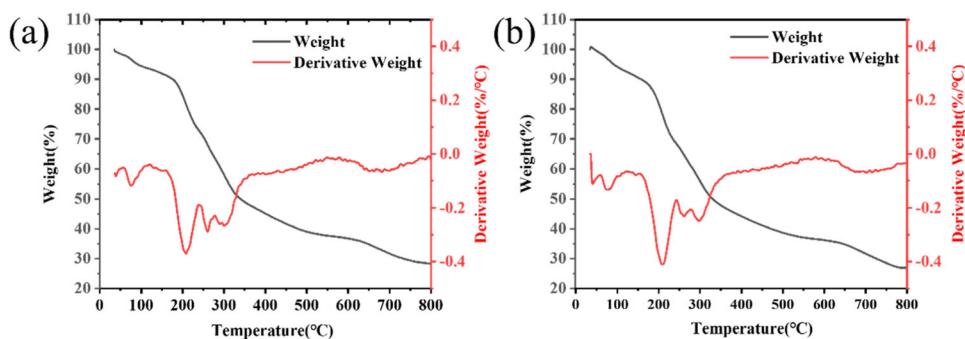
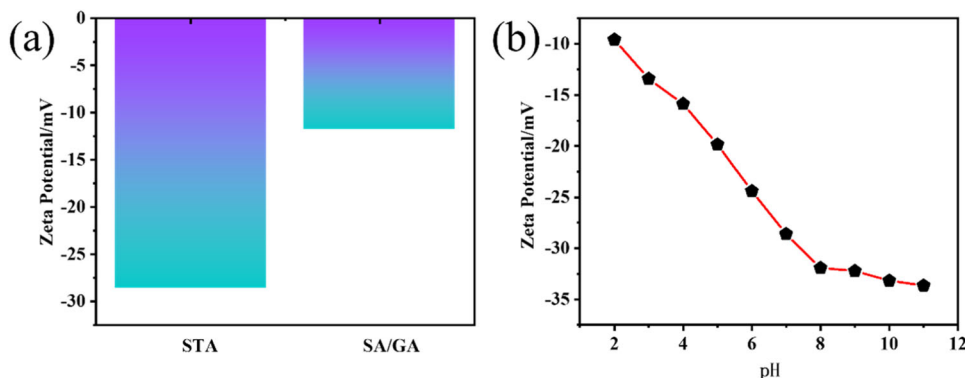


Fig. 6 a Zeta potential of STA and SA/GA under neutral conditions, **(b)** Image of the variation of Zeta potential of STA with pH value



carbonization of the matrix material, and weakened hydrogen bonding were the main causes of the second weight loss stage, which took place between 200 and 600 °C. It was between 600 and 800 °C during the third stage of weight reduction. The systemic breakdown of Ca^{2+} was the cause of the mass loss in this process. The right side of the image shows the thermogravimetric differential curve, which represents the rate of change in weight loss as a function of temperature. Further analysis reveals that the fastest thermal disintegration rate of SA/GA occurred at 205 °C while that of STA took place at 209 °C. Due to the more stable crystalline structure of cellulose in TOC, which absorbed more heat and gave it a greater decomposition temperature, the STA displayed a higher decomposition temperature. This outcome matched the data from the XRD analysis. However, additional $-\text{COOH}$ strengthened the intermolecular hydrogen bonding, making the system more stable [42]. Because SA/GA absorbed more Ca^{2+} during the process, SA/GA aerogel had a greater residual carbon rate. As a result, it included more Ca^{2+} , which ultimately increased the amount of residual carbon. In conclusion, the TOC addition helped the aerogel's thermal stabilization.

3.8 Analysis of Zeta potential

The Zeta potential of STA was examined in order to better understand the characteristics of the surface charge, and the experimental results are shown in Fig. 6. The potentials of STA and SA/GA under neutral circumstances were depicted

in Fig. 6a. Based on the comparison, it was found that STA had a lower potential and stronger negative potential, up to -28.6 mV. The TOC cross-linking reaction produced this structure. The impact of pH on the potential ground was more clearly depicted in Fig. 6b. It was clear that STA always had a negative potential, whether the environment was acidic or alkaline. But after close observation, it became clear that the curve was in a downward trend as the pH value rose. The conclusion was that the pH value increases its negative potential strength. This experiment's findings demonstrated that the STA surface was heavily charged negatively and that variations in the surroundings had an impact on the level of electronegativity. However, it is always in a condition of negative potential. As a result, electrostatic adsorption was produced when STA came into touch with cationic chemicals, which was particularly advantageous for the removal of cationic pollutants. Later adsorption experiments could confirm this finding. Through electrostatic interaction, STA with a lot of negative charges was able to adsorb with crystal violet when cationic dyes were the target of the adsorption process [43].

3.9 Analysis of adsorption experiment results

3.9.1 Standard curve analysis

The UV absorption spectrum of the CV solution was displayed in Fig. 7a, with the greatest absorption peak

Fig. 7 **a** UV absorption spectra of CV at different concentrations; **(b)** Standard curve of CV concentration vs. absorbance

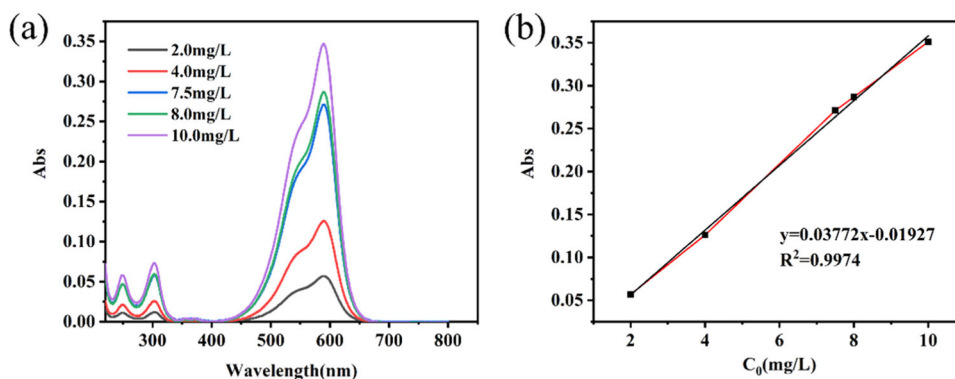
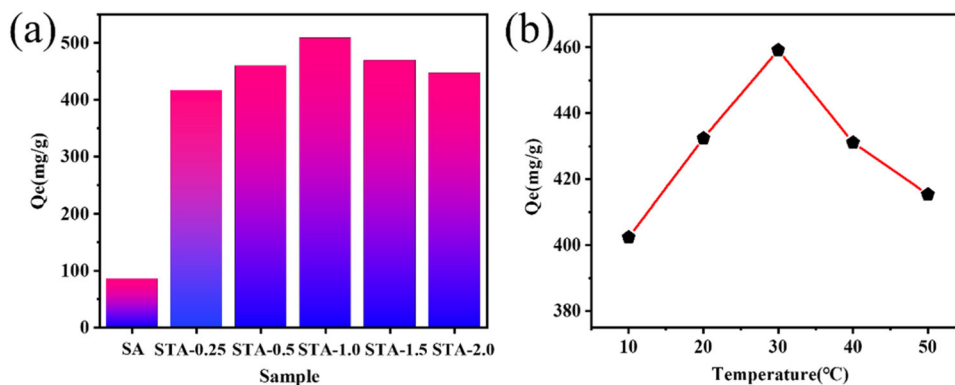


Fig. 8 **a** Equilibrium adsorption capacity of different aerogels; **(b)** Equilibrium adsorption amount of STA-1.0 on CV as a function of temperature



matching the absorption wavelength of 589 nm. The standard curve of concentration versus absorbance at 589 nm wavelength was shown in Fig. 7b. The curve has a good linear relationship, as seen by the straight line that just passed through the origin and $R^2 = 0.9974$. This standard curve was used to calculate the concentrations of the solutions before and after adsorption in the experiments that followed.

3.9.2 Analysis of adsorption results with different adsorbents

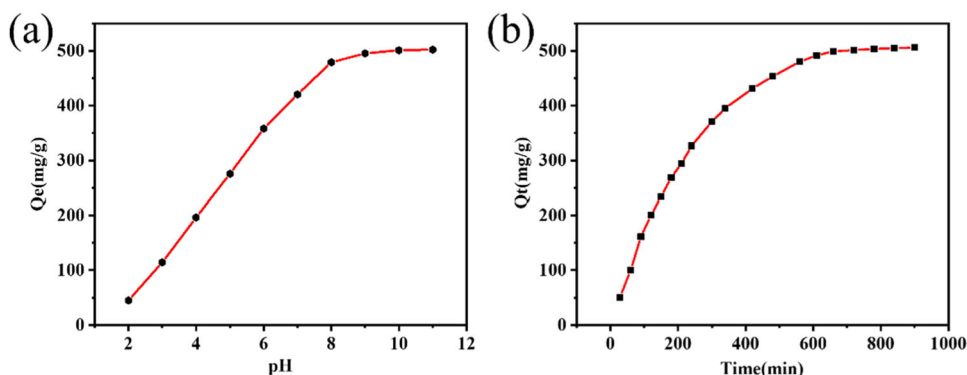
The adsorption effect in the adsorption investigations is directly influenced by the different adsorbents [44, 45]. Different TOC additions in this study lead to different adsorption capabilities. As a result, it's critical to assess each STA ratio's adsorption effectiveness on CV while keeping everything else unchanged. As can be shown in Fig. 8a below, the adsorption quantity of pure SA aerogel on CV was found to be lowest when no TOC was added, only 85.6 mg/g. This resulted from the small specific surface area, low amount of -COOH, and poor dispersion of SA. The adsorption of STA on CV then showed a trend of rising and subsequently dropping with an increase in TOC addition, and the maximum adsorption of STA was 505.9 mg/g when the TOC addition was 1%. This outcome was brought about by the greater system dispersion brought

about by the addition of TOC, which increased the specific surface area. In addition, TOC carried a lot of -COOH, which meant that there were a lot of binding sites available. When the TOC concentration was too high, it would interfere with the pore structure's development and occupy the adsorption sites, which further reduced the amount of adsorption. As a result, STA-1.0 was selected as the standard adsorbent for the adsorption tests in the subsequent investigations.

3.9.3 Effect of temperature

The amounts of adsorbed STA-1.0 on CV were investigated and studied at different temperatures to have a better understanding of STA's thermodynamic adsorption behavior on CV. The data in Fig. 8b show that at temperatures between 10 and 30 °C, the amount of adsorption increased with temperature, rising from 402.4 mg/g to 459.2 mg/g. The adsorption action was negatively impacted by temperatures that rose over this range. According to the statistics above, adsorption is more encouraged by temperature increases at lower temperatures; however, as temperatures rise beyond 30 °C, adsorption is reduced by the high temperature. The analysis showed that the explanation for this was that the temperature increase promoted the mobility of dye molecules when the temperature stayed below 30 °C. This component accelerated the adsorption of STA onto CV

Fig. 9 **(a)** Image of equilibrium adsorption of STA-1.0 on CV as a function of pH; **(b)** Image of the adsorption amount of STA-1.0 on CV with time



and raised the adsorption efficiency. The STA's interior structure would, however, sustain some damage from temperature increases that were too great. Furthermore, the higher temperature did not promote the immobilization of dye molecules at the adsorption sites, which eventually leads to a decrease in the amount of adsorption [46].

3.9.4 Effect of pH

Figure 9a displays the outcomes of STA's adsorption on CV under various pH settings. It was evident that STA-1.0's adsorption amount on CV increased from 45.1 mg/g to 420.4 mg/g while pH in the range of 2–7 gradually increased. The results made it clear that the solution's pH had a significant impact on the adsorption effect in the range. However, with subsequent pH increased, the rate of increase in adsorption quantity became exceedingly slow. The adsorption amount changed less when the pH was higher. The reason, according to the data above, was that there were many hydrogen ions present throughout the system when the pH of the solution was lower than 7. The protonation of STA would result in a reduced electrostatic interaction with the CV. The protonation was diminished as the pH continued to rise, which had the effect of gradually increasing the adsorption quantity. More negative charges were exposed on the STA's surface and inside if the pH of the system exceeded 7, increasing the number of adsorption sites. The hydrogen bonding between the adsorbent and the adsorbate was another factor contributing to the rise in the amount of adsorption at the same time as the electrostatic interaction between the STA and the CV became more apparent. There was not a noticeable increase in the quantity of adsorption, though, as more negative ions entered the solution as the pH rose and stopped the dye from sticking. This result was also supported by the Zeta potential study's findings. One of the subsequent study settings, the neutral system, was chosen to better control the experimental conditions and replicate a more realistic scenario including contaminated water [47].

3.9.5 Effect of adsorption time

The absorbance was measured over the course of 900 min at various time intervals to determine the concentration at various periods in order to account for the effects of time on the adsorption effect [48]. According to Fig. 9b, the adsorption in the 30–600 time-horizon showed a progressive rise over time. This was caused by the fact that the porous structure inside the STA portion had a lot of adsorption sites during the early stages of adsorption, which led to a significant increase in the amount of adsorption. The maximum adsorption amount was attained at 505.9 mg/g after 600 min, when the adsorption process eventually stopped altering. This outcome was caused by a decrease in the concentration of CV, a weakening of the electrostatic force, and a dynamic balance between adsorption and desorption [49].

3.9.6 Analysis of adsorption kinetics

In order to better examine the adsorption process and mechanism, the adsorption test process was analyzed and researched using pseudo-first-order and pseudo-second-order kinetic models, respectively [50]. Figure 10a, b showed the fitting results, and Table 2 showed the exact fitting parameters. Based on observation, the quasi-second-order kinetic model fit the data better, with an R^2 value closer to 1. This indicated a better linear relationship to explain the adsorption kinetics. Nevertheless, after fitting, the images derived from the quasi-first-order kinetic model showed a poorer linear correlation and were unable to adequately represent the adsorption process [51]. Additionally, the experimental value of 505.9 mg/g was more closely matched by the maximum adsorption amount (568.2 mg/g) obtained by the pseudo-second-order kinetic fit. Hence, it could be determined that the adsorption of CV by STA was a chemisorption process and related to the quasi-second-order kinetic model [52].

Fig. 10 a, b Pseudo-first-order kinetic fitting curve and pseudo-second-order kinetic fitting curve

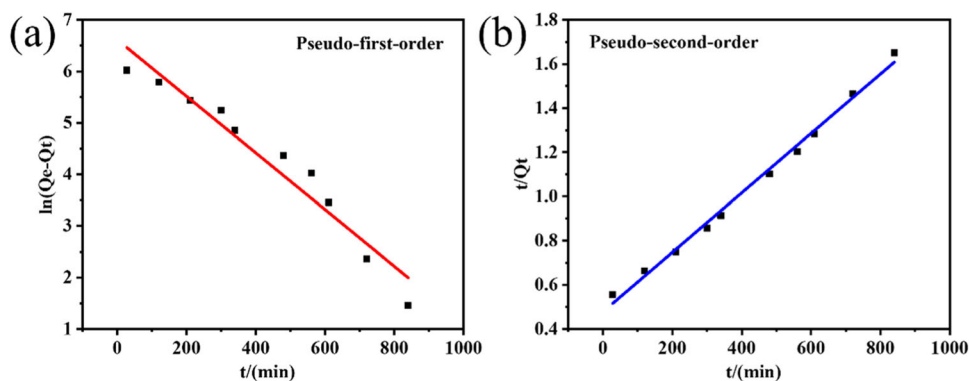


Table 2 Adsorption kinetic parameters of STA-1.0 on CV

Kinetic model	Parameter	Values
Pseudo-first-order kinetic	K_1 (g/mg min)	-0.0055
	Q_e (mg/g)	746.26
	R^2	0.9451
Pseudo-second-order kinetic	K_2 (g/mg min)	6.48×10^{-6}
	Q_e (mg/g)	568.18
	R^2	0.9967

3.9.7 Analysis of adsorption isotherm

The adsorption isotherm approach can be used to study the connection between adsorbent concentration and adsorption capabilities [53]. A curve illustrating the relationship between different initial concentrations and the amount of adsorption at the same temperature is presented in Fig. 11a. It demonstrated a pattern of inferring a favorable correlation. On the other hand, when the concentration was low, comparison revealed that the adsorption quantity exhibited a fast rising tendency with the increase of the starting concentration. The rate of increase in adsorption quantity slowed down as concentration increased, indicating that the effect of concentration started to fade after the initial concentration reached 320.0 mg/L. Regardless of concentration, adsorption saturation was eventually reached and stayed constant. During the adsorption process, sites inside and on the surface of the adsorbent were gradually occupied. Faster and more efficient binding of the dye molecules to the adsorbent and a more pronounced shift in the amount of adsorption resulted from less intense rivalry between the dye molecules and a greater number of accessible adsorption sites at lower concentrations. Adsorption became saturated as a result of increased competition among adsorbents, which prevented the limited number of adsorption sites from being able to adsorb enough dye molecules as the concentration rose [54].

The adsorption isothermal model was used to fit and analyze the experimental results. Figure 11b depicts the

outcomes of fitting the Langmuir isothermal adsorption model. It was obvious that the experimentally acquired results have better linearity compared to the Freundlich model, which produced a more dispersed scattering of numerical values and did not exhibit improved linearity. It was clear from Table 3 specific fitted values that the Langmuir correlation coefficient was getting closer to 1, indicating a more linear relationship. Additionally, the maximum adsorption capacity predicted by this model was more in line with the outcomes of the experiments. As an outcome, the Langmuir adsorption isotherm model was able to provide a more comprehensive explanation of the STA on CV monomolecular layer adsorption process. The specific fitted parameters were shown in Table 3, and it was clear that the Langmuir correlation coefficient remained near to 1, indicating that the adsorption process was simpler [55].

3.9.8 Analysis of cyclic adsorption performance

The cyclic adsorption performance of the adsorbent is an essential indicator of the adsorption performance, which reveals the reusable level and economy of the adsorbent [55]. Figure 11d illustrates the change of adsorption amount after multiple adsorption-desorption of STA-1.0. It was obvious to see that after five adsorption-desorption processes, the adsorption amount decreased from 505.9 mg/g to 433.1 mg/g, a decrease rate of about 14.4%, which reflected a relatively good adsorption capacity of the aerogel. It was very significant for the expansion of the adsorption field.

Additionally, in order to better illustrate the excellent adsorption capacity of STA, we have listed some literature for comparative analysis. The results are shown in the following table. We could find that STA shows better adsorption capacity than other aerogels of the same type Table 4.

3.9.9 Analysis of competitive adsorption

We added Cu^{2+} and Pb^{2+} as adsorption-interfering variables to the crystalline violet solutions at varying pH levels

Fig. 11 **a** Effect of initial concentration of CV on the adsorption amount of STA-1.0; **(b, c)** Langmuir and Freundlich isothermal adsorption model fitted curve; **(d)** Cyclic adsorption of STA-1.0

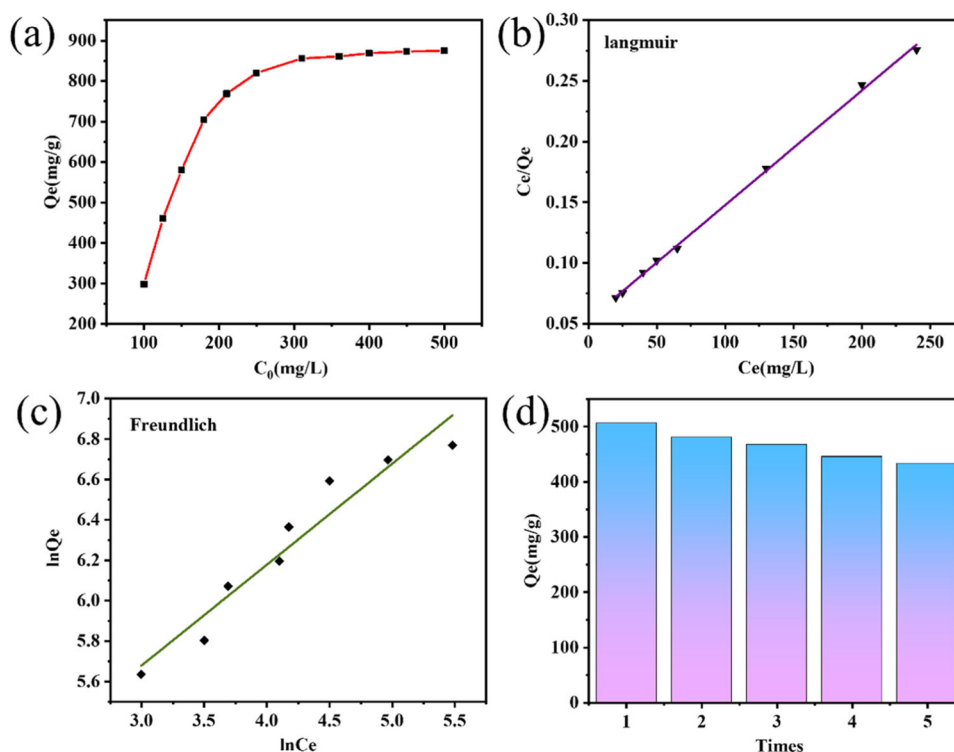


Table 3 Adsorption isotherm model parameters

Kinetic model	Parameter	Values
Langmuir	K_L (L/mg)	0.0178
	Q_m (mg/g)	1057.82
	R^2	0.9987
	R_L	0.1201–0.5618
Freundlich	K_F (mg/g)	65.37
	$1/n$	0.4981
	R^2	0.9329

Table 4 Adsorption capacity of different aerogels

Aerogels	Adsorption capacity(mg/g)	Dyes	Values
SA/CMC	7.2	Methyl blue	[56]
MSC-P	203.9	Congo red	[57]
SA/CNF/PEI	307.5	Congo red	[58]
SPCP	346.3	Congo red	[59]
SG/GO	322.6	Methyl blue	[60]
Zn-BCA	39.0	Crystal violet	[61]
PMCS-CP	78.1	Orange II	[62]

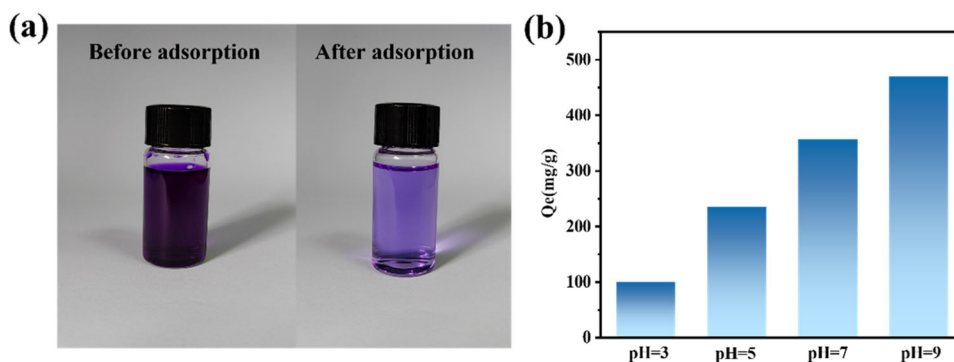
to better mimic the real industrial wastewater environment. by deciding to investigate the adsorption capability of STA-1.0 on CV. Figure 12 displayed the outcomes of the experiment. The observation of Fig. 12a indicates a substantial change in the hue of the CV solution upon adsorption. This phenomena suggests that STA has a strong

ability for CV adsorption. Furthermore, Fig. 12b shows the quantity of STA that was adsorbed on CV at various pH values. The lowest amount of adsorption, only 98.7 mg/g, was seen at pH = 3. The maximum quantity of STA that was adsorbed on CV was 469.2 mg/g, and this amount increased as the pH rose. This pattern was in line with what would have happened in the absence of Cu^{2+} and Pb^{2+} . In contrast, it was discovered that the addition of Pb^{2+} and Cu^{2+} reduced the quantity of adsorption somewhat but left it at a high level. This could be as a result of Cu^{2+} and Pb^{2+} occupying a portion of the STA adsorption sites via chelating and electrostatic interactions, which decreased the quantity of STA that was adsorbed on CV.

3.9.10 Analysis of the adsorption mechanism

The distinct chemical structures of SA and TOC enable the efficient adsorption of CV. Because of the presence of -OH and -COOH in their molecular structures, this advantage not only provides the possibility for excellent cross-linking of STA but also provides adsorption sites for effective adsorption of CV. As a cationic dye, CV can, on the one hand, be electrostatically attracted to the -COO- in STA. However, the nitrogen atoms in CV are also connected to -OH by hydrogen bonding interactions. As a result, physical adsorption is the primary mode of adsorption. These distinct benefits establish the framework for STA's high adsorption capability. Lastly, a spatial advantage for the enhancement of adsorption

Fig. 12 **a** The image of adsorption effect at pH = 9, **(b)** Curve of the adsorption capacity of STA-1.0 on CV with pH when Cu^{2+} and Pb^{2+} are added



capacity is provided by the three-dimensional porous structure of the STA [63].

4 Conclusion

In this study, we innovatively combined SA and TOC to create an aerogel with a porous structure, high thermal stability, and adsorption capabilities in a straightforward way. Under the combined cross-linking effects of calcium ions and glutaraldehyde, the SA was successfully produced. Comprehensive XPS, FTIR, and XRD analyses of the chemical makeup of STA revealed that the chemical process had been effectively completed. SEM was used to analyze the microstructure of STA, and it was discovered that the internal pore structure was clear. Using TG, the thermal stability was examined. The inclusion of TOC significantly improved the thermal stability, and the maximum porosity was 95.6%. Zeta potential analysis was used to analyze the charge characteristic. The highest adsorption quantity of CV could reach 505.9 mg/g after the adsorption properties of STA were thoroughly examined by adjusting various adsorption circumstances using adsorption kinetic and isotherm models. The thermodynamic process was closer to the fitting Langmuir results and the kinetic process was consistent with the pseudo-second-order kinetic model, indicating that the adsorption process related to single-molecule layer chemisorption. The amount of CV that was adsorbed dropped less after five adsorption-desorption cycles, and competitive adsorption also showed a satisfactory result. The mechanism of effective CV adsorption by STA was next examined and. The current work offers an effective technique for the elimination of cationic contaminants.

Acknowledgements This research did not obtain any specific grant from funding agencies in the public, commercial, or not-for-profit sectors. This research was grateful for the testing services provided by the Analysis and Testing Center of East China University of Science and Technology, Materials Research Testing Platform of Materials School.

Author contributions ZZ: conceptualization, methodology, software, writing review & editing - original draft. JW: communication, supervision, polish, project administration, funding acquisition. KL: validation, investigation. WD: data curation, investigation. XZ: investigation, polish. ZW: supervision.

Compliance with ethical standards

Conflict of interest The authors declare no competing interests.

References

- Dong T, Tian N, Xu B (2022) Biomass poplar catkin fiber-based superhydrophobic aerogel with tubular-lamellar interweaved neurons-like structure. *J Hazard Mater* 429. <https://doi.org/10.1016/j.jhazmat.2022.128290>.
- Schroeter B, Yonkova VP, Niemeyer NAM (2021) Cellulose aerogel particles: control of particle and textural properties in jet cutting process *Cellulose* 28:223–239. <https://doi.org/10.1007/s10570-020-03555-2>
- Sharma PR, Sharma SK, Antoine R (2019) Efficient removal of arsenic using zinc oxide nanocrystal-decorated regenerated microfibrillated cellulose scaffolds. *ACS Sustain Chem Eng* 7(6):6140–6151. <https://doi.org/10.1021/acssuschemeng.8b06356>
- Park M, Lee DJ, Hyun JH (2015) Nanocellulose-alginate hydrogel for cell encapsulation. *Carbohydr Polym* 116:223–228. <https://doi.org/10.1016/j.carbpol.2014.07.059>
- Jiang YH, Zhang YQ, Wang ZH (2022) Cotton-derived green sustainable membrane with tailored wettability interface: Synergy of lignin and ethyl cellulose. *Ind Crop Prod* 183. <https://doi.org/10.1016/j.indcrop.2022.114993>.
- Sharma PR, Chattopadhyay A, Zhan CB (2018) Lead removal from water using carboxycellulose nanofibers prepared by nitro-oxidation method *Cellulose* 25(3):1961–1973. <https://doi.org/10.1007/s10570-018-1659-9>
- Jiao CL, Li TT, Wang J (2020) Efficient removal of dyes from aqueous solution by a porous sodium alginate/gelatin/graphene oxide triple-network composite aerogel. *J Polym Environ* 28:1492–1502. <https://doi.org/10.1007/s10924-020-01702-1>
- Deng WF, Tang YJ, Mao JC (2021) Cellulose nanofibril as a crosslinker to reinforce the sodium alginate/chitosan hydrogels. *Cellulose* 190:890–899. <https://doi.org/10.1016/j.ijbiomac.2021.08.172>
- Guo X, Zhao H, Qiang XH (2023) Facile construction of agar-based fire-resistant aerogels: a synergistic strategy via in situ generations of magnesium hydroxide and cross-linked Ca-alginate. *Int J Biol Macromol* 227:297–306. <https://doi.org/10.1016/j.ijbiomac.2022.12.164>

10. Storer DP, Phelps JL, Wu X (2020) Rice-straw-fiber-based 3d photothermal aerogels for highly efficient solar evaporation. *ACS Appl Mater Interfaces* 12:15279–15287. <https://doi.org/10.1021/acami.0c01707>
11. Hao X, Yang, SY, Tao E (2022) High efficiency and selective removal of Cu(II) via regulating the pore size of graphene oxide/montmorillonite composite aerogel. *J Hazard Mater* 424. <https://doi.org/10.1016/j.jhazmat.2021.127680>.
12. El-Sayed NS, Kiey SAA, Darwish A (2022) High performance hydrogel electrodes based on sodium alginate-g-poly (AM-c o-ECA-co-AMPS for supercapacitor application. *Int J Biol Macromol* 218:420–430
13. Chen H, Sharma PR, Sharma SK (2022) Effective Thallium(I) Removal by Nanocellulose Bioadsorbent Prepared by Nitro-Oxidation of Sorghum Stalks. *Nanomaterials*. 12 (23). <https://doi.org/10.1016/j.carbpol.2020.116348>.
14. Xie Q, Zou YK, Wang YZ (2022) Mechanically robust sodium alginate/cellulose nanofibers/polyethyleneimine composite aerogel for effective removal of hexavalent chromium and anionic dyes. *Polym Eng Sci* 62:1927–1940. <https://doi.org/10.1002/pen.25976>
15. Li WQ, Zhang LP, Hu D (2021) A mesoporous nanocellulose/sodium alginate/carboxymethyl-chitosan gel beads for efficient adsorption of Cu²⁺ and Pb²⁺. *Int J Biol Macromol* 187(2021):922–930. <https://doi.org/10.1016/j.ijbiomac.2021.07.181>
16. Zhu G, Isaza LG, Huang B (2022) Multifunctional nanocellulose/carbon nanotube composite aerogels for high-efficiency electromagnetic interference shielding. *ACS Sustain Chem Eng* 10:2397–2408. <https://doi.org/10.1021/acssuschemeng.1c07148>
17. Karimzadeh Z, Namazi H (2022) Nontoxic double-network polymeric hybrid aerogel functionalized with reduced graphene oxide: Preparation, characterization, and evaluation as drug delivery agent. *J Polym Res* 29. <https://doi.org/10.1007/s10965-022-02902-0>.
18. Long LY, Li FF, Weng YX (2019) Effects of sodium montmorillonite on the preparation and properties of cellulose aerogels. *Polymers* 11. <https://doi.org/10.3390/polym11030415>.
19. Sharma PR, Chattopadhyay A, Sharma S (2017) Efficient removal of UO₂²⁺ from water using carboxycellulose nanofibers prepared by the nitro-oxidation method. *Ind Eng Chem Res* 56(46):13885–13893. <https://doi.org/10.1021/acs.iecr.7b03659>
20. Das R, Lindström T, Sharma PR (2022) Nanocellulose for sustainable water purification. *Chem Rev* 122(9):8936–9031. <https://doi.org/10.1021/acs.chemrev.1c00683>
21. Liu QY, Liu YQ, Feng Q (2023) Preparation of antifouling and highly hydrophobic cellulose nanofibers/alginate aerogels by bidirectional freeze-drying for water-oil separation in the ocean environment. *J Hazard Mater* 44. <https://doi.org/10.1016/j.jhazmat.2022.129965>.
22. Yang J, Xia YF, Xu P (2018) Super-elastic and highly hydrophobic/superoleophilic sodium alginate/cellulose aerogel for oil/water separation. *Cellulose* 25:3533–3544. <https://doi.org/10.1007/s10570-018-1801-8>
23. Sharma PR, Joshi R, Sharma SK (2017) A simple approach to prepare carboxycellulose nanofibers from untreated biomass. *Biomacromolecules* 18(8):2333–2342. <https://doi.org/10.1021/acs.biomac.7b00544>
24. Liu CY, Liu HY, Xu AR (2017) In situ reduced and assembled three-dimensional graphene aerogel for efficient dye removal. *J Alloy Compd* 714:522–529. <https://doi.org/10.1016/j.jallcom.2017.04.245>
25. Zhang YF, Wu L, Deng HL (2021) Modified graphene oxide composite aerogels for enhanced adsorption behavior to heavy metal ions. *J Environ Chem Eng* 9. <https://doi.org/10.1016/j.jece.2021.106008>.
26. Han XH, Liang JC, Fukuda S (2022) Sodium alginate-silica composite aerogels from rice husk ash for efficient absorption of organic pollutants. *Biomass Bioenerg* 159. <https://doi.org/10.1016/j.biombioe.2022.106424>.
27. Tian YR, Zhang XF, Feng XY (2021) Shapeable and underwater super-elastic cellulose nanofiber/alginate cryogels by freezing-induced oxa-Michael reaction for efficient protein purification. *Carbohydr Polym* 27. <https://doi.org/10.1016/j.carbpol.2021.118498>.
28. Gao C, Wang XL, An QD (2021) Synergistic preparation of modified alginate aerogel with melamine/chitosan for efficiently selective adsorption of lead ions. *Carbohydr Polym* 25. <https://doi.org/10.1016/j.carbpol.2020.117564>.
29. Wang ZQ, Wu SS, Zhang YN (2020) Preparation of modified sodium alginate aerogel and its application in removing lead and cadmium ions in wastewater. *Int J Biol Macromol* 157:687–694. <https://doi.org/10.1016/j.ijbiomac.2019.11.228>
30. Wang SK, Ma XF, Zheng PW (2019) Sulfo-functional 3D porous cellulose/graphene oxide composites for highly efficient removal of methylene blue and tetracycline from water. *Int J Biol Macromol* 140:119–128. <https://doi.org/10.1016/j.ijbiomac.2019.08.111>
31. Feng JZ, Su BL, Xia HS (2021) Printed aerogels: chemistry, processing, and applications. *Chem Soc Rev* 50:3842–3888. <https://doi.org/10.1039/c9cs00757a>
32. Wang FF, Zhang H, Sun YF (2023) Superhydrophilic quaternized calcium alginate based aerogel membrane for oil-water separation and removal of bacteria and dyes. *Int J Biol Macromol* 227:1141–1150. <https://doi.org/10.1016/j.ijbiomac.2022.11.294>
33. Wang M, Yang Q, Zhao XQ (2019) Highly efficient removal of copper ions from water by using a novel alginate-polyethyleneimine hybrid aerogel. *Int J Biol Macromol* 138:1079–1086. <https://doi.org/10.1016/j.ijbiomac.2019.07.160>
34. Feng YL, Wang H, Xu JH (2021) Fabrication of MXene/PEI functionalized sodium alginate aerogel and its excellent adsorption behavior for Cr(VI) and Congo Red from aqueous solution. *J Hazard Mater* 416. <https://doi.org/10.1016/j.jhazmat.2021.125777>.
35. Rong NN, Chen CC, Ouyang KW (2021) Adsorption characteristics of directional cellulose nanofiber/chitosan/ montmorillonite aerogel as adsorbent for wastewater treatment. *Sep Purif Technol* 274. <https://doi.org/10.1016/j.seppur.2021.119120>.
36. Zheng K, Gong WL, Wu MB (2023) Amphoteric cellulose microspheres for the efficient remediation of anionic and cationic dyeing wastewater. *Sep Purif Technol* 309. <https://doi.org/10.1016/j.seppur.2022.123035>.
37. Guo WH, Zhang JB, Yang F (2020) Highly efficient and selective recovery of gallium achieved on an amide-functionalized cellulose. *Sep Purif Technol* 23. <https://doi.org/10.1016/j.seppur.2019.116355>.
38. He XX, Sun CX, Khalesi HD (2022) Comparison of cellulose derivatives for Ca²⁺ and Zn²⁺ adsorption: Binding behavior and in vivo bioavailability. *Carbohydr Polym* 294. <https://doi.org/10.1016/j.carbpol.2022.119837>.
39. Wang Y, Li YX, Zhang YP (2021) Nanocellulose aerogel for highly efficient adsorption of uranium (VI) from aqueous solution. *Carbohydr Polym* 267. <https://doi.org/10.1016/j.carbpol.2021.118233>.
40. Zhou SJ, Xia LJ, Fu Z (2021) Purification of dye-contaminated ethanol-water mixture using magnetic cellulose powders derived from agricultural waste biomass. *Carbohydr Polym* 258. <https://doi.org/10.1016/j.carbpol.2021.117690>.
41. Zhang TM, Zhang WW, Xi H (2021) Polydopamine functionalized cellulose-MXene composite aerogel with superior adsorption of methylene blue. *Cellulose* 28:4281–4293. <https://doi.org/10.1007/s10570-021-03737-6>

42. Cheng TJ, Zhang YH, Cui FJ (2022) Preparation of novel ZIF-8 aerogel adsorbent based on cellulose and the application of Cu (II) removal from wastewater. *Chem Phys Lett* 808. <https://doi.org/10.1016/j.cplett.2022.140100>.
43. Dilamian M, Noroozi B (2021) Rice straw agri-waste for water pollutant adsorption: Relevant mesoporous super hydrophobic cellulose aerogel. *Carbohydr Polym* 251. <https://doi.org/10.1016/j.carbpol.2020.117016>.
44. Gao L, Li ZH, Yi WM (2023) Effective Pb²⁺ adsorption by calcium alginate/modified cotton stalk biochar aerogel spheres: with application in actual wastewater. *J Environ Chem Eng* 11. <https://doi.org/10.1016/j.jece.2022.109074>.
45. Wang XY, Xie PB, He L (2022) Ultralight, mechanically enhanced, and thermally improved graphene-cellulose-polyethyleneimine aerogels for the adsorption of anionic and cationic dyes. *Nanomater* 12. <https://doi.org/10.3390/na12101727>.
46. He BY, Zhang YY, Li BJ (2021) Preparation and hydrophobic modification of carboxymethyl chitosan aerogels and their application as an oil adsorption material. *J Environ Chem Eng* 9 <https://doi.org/10.1016/j.jece.2021.106333>.
47. Chong KY, Chia CH, Zakaria S (2015) CaCO₃-decorated cellulose aerogel for removal of Congo Red from aqueous solution. *Cellulose* 22(4):2683–2691. <https://doi.org/10.1007/s10570-015-0675-2>
48. Cui FJ, Li HD, Chen C (2021) Cattail fibers as source of cellulose to prepare a novel type of composite aerogel adsorbent for the removal of enrofloxacin in wastewater. *Int J Biol Macromol* 191:171–181. <https://doi.org/10.1016/j.ijbiomac.2021.09.022>
49. Dilamian M, Noroozi B (2021) Rice straw agri-waste for water pollutant adsorption: Relevant mesoporous super hydrophobic cellulose aerogel. *Carbohydr Polym* 25:117016. <https://doi.org/10.1016/j.carbpol.2020.117016>
50. Liu K, Chen LH, Huang LL (2018) Adsorption behaviors of acidic and basic dyes by thiourea-modified nanocomposite aerogels based on nanofibrillated cellulose. *Bioresources* 13(3):5836–5849
51. Luo MF, Wang M, Pang HP (2021) Super-assembled highly compressible and flexible cellulose aerogels for methylene blue removal from water. *Chin Chem Lett* 32(6):2091–2096. <https://doi.org/10.1016/j.cclet.2021.03.024>
52. Ren LL, Yang ZH, Huang L (2020) Macroscopic poly Schiff base-coated bacteria cellulose with high adsorption performance. *Polymers* 12(3):714. <https://doi.org/10.3390/polym12030714>
53. Wei X, Huang T, Nie J (2018) Bio-inspired functionalization of microcrystalline cellulose aerogel with high adsorption performance toward dyes. *Carbohydr Polym* 198:546–555. <https://doi.org/10.1016/j.carbpol.2018.06.112>
54. Zhang F, Wu WB, Sharma S (2015) Synthesis of cyclodextrin-functionalized cellulose nanofibril aerogel as a highly effective adsorbent for phenol pollutant removal. *Bioresources* 10(4):7555–7568
55. Zhang TM, Zhang WW, Xi H (2021) Polydopamine functionalized cellulose-MXene composite aerogel with superior adsorption of methylene blue. *Cellulose* 28(7):4281–4293. <https://doi.org/10.1007/s10570-021-03737-6>
56. Li HM, Huang JY, Shen S (2023) Superhydrophobic sodium alginate/cellulose aerogel for dye adsorption and oil-water separation. *Cellulose* 30(11):7157–7175. <https://doi.org/10.1007/s10570-023-05307-4>
57. Su HZ, Qiu WP, Deng TR (2023) Fabrication of physically multi-crosslinked sodium alginate/carboxylated-chitosan/montmorillonite-base aerogel modified by polyethyleneimine for the efficient adsorption of organic dye and Cu(II) contaminants. *Sep Purif Technol* 330:125321. <https://doi.org/10.1016/j.seppur.2023.125321>
58. Xie Q, Zou YK, Wang YZ (2022) Mechanically robust sodium alginate/cellulose nanofibers/polyethyleneimine composite aerogel for effective removal of hexavalent chromium and anionic dyes. *Polym Eng Sci* 62(6):1927–1940. <https://doi.org/10.1002/pen.25976>
59. Li J, Lei LL, Liu Z (2023) Sodium alginate/polyethyleneimine/polydopamine@cellulose nanofiber composite aerogel as a novel adsorbent for Cr(VI) and dyes removal. *Polym Eng Sci* 63(10):3492–3506. <https://doi.org/10.1002/pen.26462>
60. Jiao CL, Li TT, Wang J (2020) Efficient removal of dyes from aqueous solution by a porous sodium alginate/gelatin/graphene oxide triple-network composite aerogel. *J Polym Environ* 28(5):1492–1502. <https://doi.org/10.1007/s10924-020-01702-1>
61. Vu CL, Chau NDV, Kim HND (2023) Zinc oxide-doped carbon aerogel derived from bagasse cellulose/sodium alginate/zinc nitrate composite for dye adsorption, storage energy and electrochemical sensing. *J Chem Technol Biotechnol* <https://doi.org/10.1002/jctb.7536>
62. Chen ZC, Weng PX, Song YH (2023) Loofah-inspired sodium alginate/carboxymethyl cellulose sodium-based porous frame for all-weather super-viscous crude oil adsorption and wastewater treatment in harsh environment. *Carbohydr Polym* 323:121450. <https://doi.org/10.1016/j.carbpol.2023.121450>
63. Zhuang J, Pan MZ, Zhang YH (2023) Rapid adsorption of directional cellulose nanofibers/3-glycidoxypropyltrimethoxysilane/polyethyleneimine aerogels on microplastics in water. *Int J Biol Macromol* 235. <https://doi.org/10.1016/j.ijbiomac.2023.123884>.

Publisher's note Springer Nature remains neutral with regard to jurisdictional claims in published maps and institutional affiliations.

Springer Nature or its licensor (e.g. a society or other partner) holds exclusive rights to this article under a publishing agreement with the author(s) or other rightsholder(s); author self-archiving of the accepted manuscript version of this article is solely governed by the terms of such publishing agreement and applicable law.